

## RESEARCH ARTICLE



# Exploring the Bilayer Approach to Analyzing Lead-Free Perovskite Solar Cells' Numerical Aspects for High Efficiency

Shahid Farhan<sup>1</sup> , M. Qasim Shah<sup>2,\*</sup> , M. Naeem Khan<sup>1</sup>, M. Arif<sup>3</sup> and Asim Ghafoor<sup>2</sup>

<sup>1</sup>Department of Electrical Engineering, Government College University, Pakistan

<sup>2</sup>Department of Electronics, Government College University, Pakistan

<sup>3</sup>Department of Renewable Energy Engineering, U.S. Pakistan Center for Advanced Studies in Energy, Pakistan

**Abstract:** In the past decades, the metal halide perovskites gained tremendous attention from researchers because of its excellent visible light absorption and promising power conversion efficiencies. But due its toxic nature and concerned ecological hazards, it cannot be commercialized on a large scale. So there was a need to introduce a new toxic-free alternative. According to this paper, a volume lead-free perovskite structure is quantitatively investigated using 1D solar cell capacitance simulator (SCAPS) software. A new approach is used in which the lead-free active layer  $\text{CH}_3\text{NH}_3\text{SnI}_3$  is encased in two bilayers of a simultaneous simulation that investigates the hole transport layer and electron transport layer and fine-tunes their respective thicknesses as well as the absorber layer to attain the best possible performance for the suggested structure. Furthermore, a number of parameters influencing electrical properties were studied statistically, including the effect of different rear connections, temperature changes, doping concentration in the absorber layer, defect states at interfaces, and the overall density of defects. The optimal configuration yielded an open circuit voltage ( $V_{oc}$ ) of 0.96V, a short circuit current density ( $J_{sc}$ ) of 32 mA/cm<sup>2</sup>, a fill factor of 82.02, and a power conversion efficiency of 26.09% under standard AM1.5 G conditions.

**Keywords:** lead-free perovskites, double electron transport layer (ETL) and hole transport layer (HTL), SCAPS (1D)

## 1. Introduction

The current global trajectory is moving toward sustainable and environmentally friendly with the increasing demand for energy and the substantial expenses linked to conventional sources; there is a growing interest in alternative energy sources, polluting resources. Solar energy is more efficient, eco-friendly, and a reliable energy resource compared to other types of resources for electric power generation. According to a recent prediction, solar technology is expected to generate one-third of the world's electric power by the end of 2030 [1].

The 1G solar cells (monocrystalline and polycrystalline) made up of silicon wafers are contributing 90% to the fabrication of Photovoltaic (PV) products throughout the international market having an about 26% power conversion efficiency known as PCE [2, 3]. However, due to its very high fabrication cost and low PCE, further improvements in PCE have faced challenges due to technological and material-wise issues [4]. Solar technology is being innovated to improve the PCE. One of the most innovative/novel contributions is the third-generation perovskite-based photovoltaic cells. Throughout the last 10 years, solar cells based on perovskites have garnered appreciable curiosity among academics due to their notable power conversion efficiencies,

enhanced mobility, heightened absorption capabilities, extended diffusion durations, and cost-effective fabrication processes [5]. The efficiency of  $\text{CH}_3\text{NH}_3\text{PbX}_3$  perovskite solar cells (PSCs) has seen remarkable increase, increasing up to 25.2% in 2019 from 3.8% in 2009 [6]. The compound known as perovskite can be represented by the chemical composition  $\text{ABX}_3$ : in this case, X stands for an anion, and cations A and B come in various sizes. One of perovskite's features is that it may behave as an active layer or light harvester [7]. Methylammonium lead tri-iodide ( $\text{MAPbI}_3$ ) has been a potential candidate for its use as an absorbing layer with a tunable energy bandgap of range (1.5–2.3 eV) [8, 9]. Even though lead base PSC shows the highest efficiency which has reached nearly 23% but due to its toxic nature, instability, ecological hazards, and easy degradation with water, it cannot be commercialized on a large scale. As there was need of suitable alternative of  $\text{CH}_3\text{NH}_3\text{PbI}_3$  across the world,  $\text{CH}_3\text{NH}_3\text{SnI}_3$  is being researched due to its many features, like good stability, low energy bandgap (almost 1.3 eV), significant absorption coefficient, shorter diffusion length, and low recombination rates as compare to  $\text{CH}_3\text{NH}_3\text{PbI}_3$  [10–12].

PSCs fall into one of two main structural categories: either the (p–i–n) or (n–i–p) structure. Despite their straightforward design, planar PSCs have few interface defects and excellent internal quantum efficiency (QE). A transparent electrode (Fluorine-doped Tin Oxide (FTO) or Indium Tin Oxide (ITO)), an electron

\*Corresponding author: M. Qasim Shah, Department of Electronics, Government College University, Pakistan. Email: [m.qasim@gcu.edu.pk](mailto:m.qasim@gcu.edu.pk)

transport layer (ETL), a perovskite absorber layer, and a hole transport layer (HTL) are the essential parts of a non-inverted planar perovskite device's construction and a metal electrode. The process of separating and introducing photogenerated electron-hole pairs into a PSC's ETL and HTL is facilitated by energy gaps between successive layers in the cell's structure between this mechanism; electrons and electron vacancies are able to move between their respective electrodes, accumulating and producing a voltage ( $V_{oc}$ ) and light-induced current ( $J_{sc}$ ) [13].

Typically, a perovskite material is expected to possess both an ETL and an HTL to make it easier to retrieve and move charge carriers created by photos, hence improving the efficiency of the active layer [14, 15]. In order to ensure optimal electrical conductivity and a minimal conduction band, it is imperative that a highly efficient ETL possesses exceptional quality. Different materials are used for TiO<sub>2</sub>, ZnO, and Spiro-OMeTAD, but not for ETL and HTL, which have gained significant attention due to their promising attributes [16]. In the suggested device structure, one of the electron transport materials (ETMs) is ZnO. It is selected for its low processing temperature and high mobility, ensuring excellent carrier extraction [17, 18]. Moreover, ZnO enjoys widespread use in commercial solar cells [19]. Large-scale production of PSCs faces limitations due to the considerable expenses involved in their fabrication and the complexity of the manufacturing process [20]. There was a requirement for an alternate solution in this particular scenario. CuI, an exceptional inorganic P-type material, possesses remarkable characteristics such as a broad bandgap and high hole mobility. When CuI is doped with poly-triaryl amine [21], up to 20% PCEs are possible using PSCs.

This work offers a numerical examination of a novel method that employs TiO<sub>2</sub> and ZnO as high-efficiency PSCs by using CuI and V<sub>2</sub>O<sub>5</sub> as the HTL and the ETL. The 1D solar cell capacitance simulator (SCAPS-1D) is used to concurrently propose, optimize, and simulate bilayers of ETL and HTL in the suggested configuration. CH<sub>3</sub>NH<sub>3</sub>SnI<sub>3</sub> is the absorber layer used in the simulations. The device's total photovoltaic performance was examined in relation to various back connections, absorber layer thickness, total defect density, interface density of defect states, and operation temperature. Developing the proposed device structure in an experimental environment is the aim of this preliminary study. The following are the reasons why this structure was chosen: (1) it is more efficient and Pb-free, (2) it has an uncomplicated deposition method, and (3) the material is readily available on the market at low cost. The expected results of this research are expected to provide significant perspectives for the future research and manufacturing of lead-free PSCs, with an emphasis on their commercial feasibility.

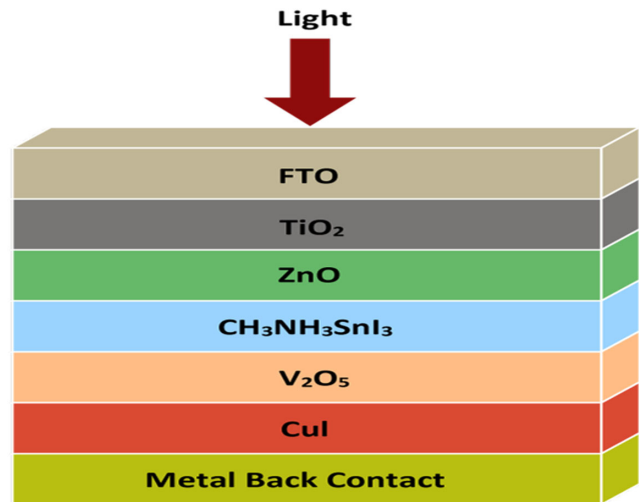
## 2. Proposed Model and Simulations

As seen in Figure 1 from upside down, Cu/CuI/V<sub>2</sub>O<sub>5</sub>/CH<sub>3</sub>NH<sub>3</sub>SnI<sub>3</sub>/ZnO/TiO<sub>2</sub>/FTO, we have presented a non-inverted planar heterojunction design for PSC. In the device design, the active layer, also known as the absorber layer, is positioned between the two layers of ETL and HTL.

Excellent ETL and HTL are necessary for maximal conductivity, and they should also have point-to-point correspondence for a high PCE. Each layer's functionalities are as follows: Because of its high mobility and low processing temperature, ZnO aids in carrier extraction [22]. Additionally, V<sub>2</sub>O<sub>5</sub> has been employed as HTL due to its suitable band configuration, high hole mobility, and increased transparency to visible light [23]. Because the compound 9, 9-bifluorene may achieve the maximum possible PCE, Spiro-OMeTAD is often used as the HTL in PSCs [16, 20].

However, the high cost of fabrication and the intricate manufacturing process of Spiro-OMeTAD hinder its utilization. An alternative for Spiro-OMeTAD in HTL applications has been suggested: copper iodide (CuI) [24].

Figure 1  
Layer scheme of the CH<sub>3</sub>NH<sub>3</sub>SnI<sub>3</sub> perovskite structure



Precise engineering is required to overcome the major manufacturing issues posed by the combination of ETL and HTL bilayers in non-inverted PSC design.

Our theoretical study underscores an optimized structure featuring CH<sub>3</sub>NH<sub>3</sub>SnI<sub>3</sub> as the absorber layer flanked by ETL (TiO<sub>2</sub>, ZnO) and HTL (CuI, V<sub>2</sub>O<sub>5</sub>) bilayers. Achieving uniform deposition among materials with distinct properties necessitates precise techniques to minimize defects and ensure optimal charge transport [25].

Controlling nanoscale thicknesses, as optimized in our simulations, requires advanced, high-precision deposition methods [16].

Addressing these challenges mandates a collaborative, multidisciplinary effort. This collaboration aims to convert theoretical optimizations into real, high-performing solar cells by creating reliable, scalable fabrication processes [16, 26–29].

## 3. Result and Discussion

Figure 2 displays the energy band diagram of the researched PSC that was simulated using SCAPS-1D. Crucial components of solar cell analysis include evaluating the PCE, fill factor ( $FF$ ), open-circuit voltage ( $V_{oc}$ ), and current density ( $J_{sc}$ ). These elements are essential to understanding how a solar cell functions and performs. Retrieving these values is made simple by SCAPS-1D software.

Consequently, we are able to understand a variety of profiles, including bandgap profiles and recombination profiles. Additionally, all measurements can be performed in both bright and dim lighting. Figure 3 shows the voltage vs current ( $J$ - $V$ ) characteristic, whereas Figure 4 displays the QE curves for the recommended device.

Using SCAPS-1D software, simulation was used to get these results. Table 1 is a list of the characteristic parameters for the suggested PSCs. The optimal layer thicknesses with PCE over 26% are 400, 50, 90, 550, 100, and 20 nm for FTO, TiO<sub>2</sub>, ZnO, CH<sub>3</sub>NH<sub>3</sub>SnI<sub>3</sub>, CuI, and V<sub>2</sub>O<sub>5</sub>, respectively.

Figure 2

Energy band versus distance diagram of  $\text{CH}_3\text{NH}_3\text{SnI}_3$  structure

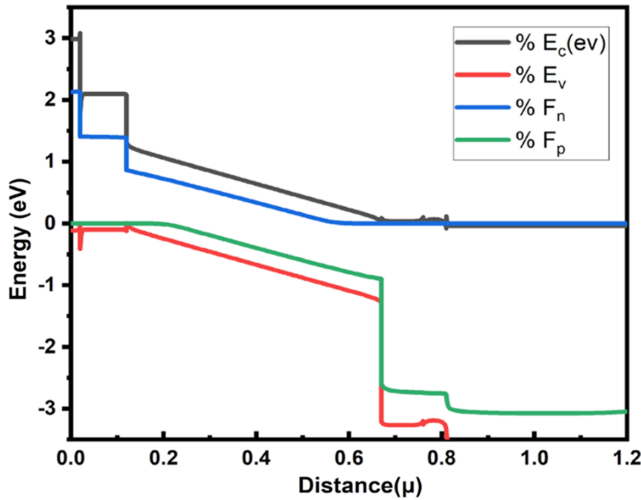
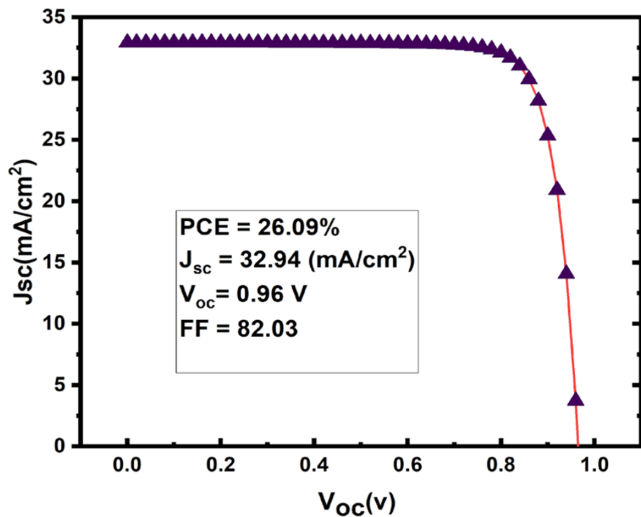


Figure 3

This perovskite structure's J-V property is  $\text{CH}_3\text{NH}_3\text{SnI}_3$

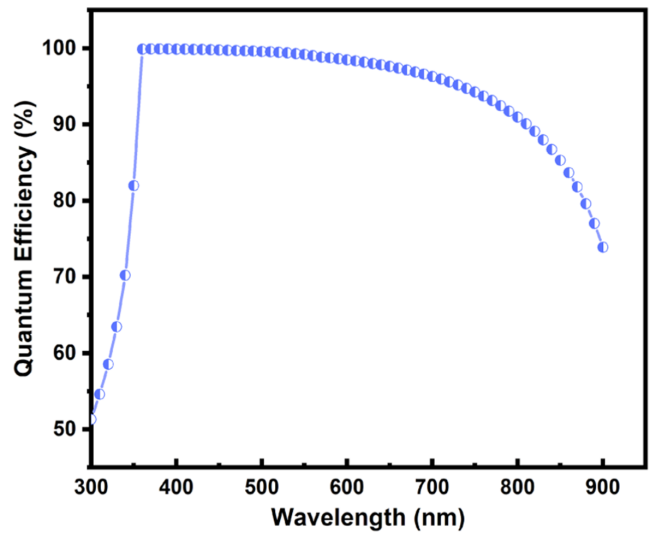


### 3.1. Simulation model

SCAPS-1D [21], which has been widely used since the early days of solar technology for numerical investigation of silicon-based solar cells CIGS and CdTe, which are known as 1 G and 2 G solar cells, respectively, is used in the current work to simulate the suggested solar cell design. It has recently drawn interest from scholars all over the world and has been widely employed for numerical analysis of novel PSC structures, both inverted and non-inverted. Three pair differential equations of semiconductors in an equilibrium situation inside a one-dimensional setting are solved using SCAPS-1D [30]. The electron continuity in Equation (3) and the hole continuity in Equation (2), together with Poisson's Equation (1), describe the fundamental charge carrier dynamics within the solar cell structure.

Figure 4

The  $\text{CH}_3\text{NH}_3\text{SnI}_3$  perovskite structure's quantum efficiency trend



$$\text{as } \frac{d}{dx} \left( -\varepsilon(x) \frac{d\Psi}{dx} \right) = q[p(x) - n(x) + N_d^+(x) - N_a^-(x) + p_t(x) - n_t(x)] \quad (1)$$

$$\frac{dp_n}{dt} = G_p - \frac{p_n - p_{n0}}{\tau_p} - p_n \mu_p \frac{d\xi}{dx} - \mu_p \xi \frac{dp_n}{dx} + D_p \frac{d^2 p_n}{dx^2} \quad (2)$$

$$\frac{dn_p}{dt} = G_n - \frac{n_p - n_{p0}}{\tau_p} - n_p \mu_n \frac{d\xi}{dx} - \mu_n \xi \frac{dn_p}{dx} + D_n \frac{d^2 n_p}{dx^2} \quad (3)$$

The electrostatic potential is denoted by  $\Psi$  in this context, together with the dielectric constant ( $\varepsilon$ ), electron charge ( $q$ ), permittivity of empty space ( $\varepsilon_0$ ), diffusion coefficient ( $D$ ), and quantities of trapped electrons, free holes, and free electrons ( $n$ ,  $p$ ,  $n_t$ , and  $p_t$ , respectively). The symbol "Na-" denotes the presence of ionized acceptor-like doping, whereas the symbol "Nd+" indicates the presence of ionized donor-like doping.

The electrical and optical parameter values are derived from appropriate literature sources, experimental studies, and theoretical models. Tables 1 and 2 have been created from the compilation of these values. The device simulations were performed at 300 Kelvin and normal AM 1.5 G conditions.

### 3.2. Influence of absorber layer thickness on electrical characteristics

The thickness of the absorber layer has a significant effect on the performance of solar cells. This layer has an important influence on the PCE,  $FF$ , open-circuit voltage ( $V_{oc}$ ), short-circuit current density ( $J_{sc}$ ), and other crucial electrical characteristics of PSCs. Its most notable consequence is its effect on the charge carrier diffusion length.

Table 1

The parameters employed for the modeling of these are the results of using the SCAPS-1D program to create an inverted perovskite solar cell

Parameters	FTO	TiO <sub>2</sub> (ETL)	ZnO (ETL)	CH <sub>3</sub> NH <sub>3</sub> SnI <sub>3</sub>	V <sub>2</sub> O <sub>5</sub> (HTL)	CuI (HTL)
Thickness (in nm)	400	50	90	550	100	20
Permittivity-dielectric (considered relative)	9.0	9.0	9.0	10.00	8.00	6.50
(In eV) electron affinity	4.0	4.20	4.1	4.17	3.40	2.10
Bandgap (eV)	3.50	3.26	3.3	1.3	2.20	3.10
Effective density of states for VB, measured in 1/cm <sup>2</sup>	1.8 × 10 <sup>18</sup>	1.8 × 10 <sup>18</sup>	1.0 × 10 <sup>19</sup>	1.8 × 10 <sup>18</sup>	5.0 × 10 <sup>20</sup>	2.5 × 10 <sup>20</sup>
1/cm <sup>3</sup> is the States' effective density of CB	2.2 × 10 <sup>18</sup>	2.2 × 10 <sup>18</sup>	4.0 × 10 <sup>18</sup>	2.2 × 10 <sup>18</sup>	9.2 × 10 <sup>19</sup>	2.5 × 10 <sup>20</sup>
Thermal speed through the hole, measured in cm/s	1.00 × 10 <sup>7</sup>	1.00 × 10 <sup>7</sup>	1.0 × 10 <sup>7</sup>	1.0 × 10 <sup>7</sup>	1.0 × 10 <sup>7</sup>	1.0 × 10 <sup>7</sup>
Electron temperature velocity (in cm/s)	1.00 × 10 <sup>7</sup>	1.00 × 10 <sup>7</sup>	1.0 × 10 <sup>7</sup>	1.0 × 10 <sup>7</sup>	1.0 × 10 <sup>7</sup>	1.0 × 10 <sup>7</sup>
Measured in cm <sup>2</sup> /Vs, hole mobility	1.00 × 10	1.00 × 10	2.50 × 10	1.60	1.0 × 10 <sup>2</sup>	4.40
Mobility of electrons (in cm <sup>2</sup> /Vs)	2.00 × 10	2.00 × 10	1.0 × 10 <sup>2</sup>	1.60	1.5 × 10 <sup>2</sup>	4.40
NA (1/cm <sup>3</sup> ), the shallow uniform acceptor density	1.00 × 10 <sup>19</sup>	1.00 × 10 <sup>17</sup>	1.00 × 10 <sup>18</sup>	0.00	0.00	0.00
Neutral acceptor density at shallow depths, NA (1/cm <sup>3</sup> )	0.00	0.00	0.00	0.00	1.0 × 10 <sup>19</sup>	3.0 × 10 <sup>18</sup>
Type of defect	Neutral	Neutral	Neutral	Neutral	Neutral	Neutral
Hole capture for the cross section (cm <sup>2</sup> )	1 × 10 <sup>-15</sup>	1 × 10 <sup>-15</sup>	1 × 10 <sup>-15</sup>			
Captured electron cross section (cm <sup>2</sup> )	1 × 10 <sup>-15</sup>	1 × 10 <sup>-15</sup>	1 × 10 <sup>-15</sup>			
Origin of fault et's energy level	Above E <sub>v</sub>	Above E <sub>v</sub>	Above E <sub>v</sub>	Above E <sub>v</sub>	Above E <sub>v</sub>	Above E <sub>v</sub>
Distribution of energies	Single	Single	Single	Single	Single	Single
Nt total (in 1/cm <sup>3</sup> ) consistent Energy	1 × 10 <sup>15</sup>	1 × 10 <sup>15</sup>	1 × 10 <sup>15</sup>	3.0 × 10 <sup>14</sup>	1 × 10 <sup>15</sup>	1 × 10 <sup>15</sup>
Energy level in eV relative to the reference	0.600	0.600	0.600	0.600	0.600	0.600

Table 2  
Different back contact metal's effects

Metal back in contact	Sn	Ag	Fe	Cu	Au
Function of metal work in (eV)	4.42	4.74	4.81	5.0	5.12

This round of the simulations involved adjusting the thickness of the active layer between 0 and 1600 nm. There was no change in the thickness of the remaining layers, which were 400 nm for FTO, 90 nm and 50 nm for ETL, and 100 nm and 20 nm for HTL. The dependence of  $J_{sc}$  on the thickness of the perovskite absorber layer is seen in Figure 5(a).  $J_{sc}$  increases quickly as the active layer thickness increases, peaking at 35.23 mA/cm<sup>2</sup> at 750 nm layer thickness, from 8.9 mA/cm<sup>2</sup> at baseline. In terms of electrical properties,  $J_{sc}$  is optimized at 32.94 mA/cm<sup>2</sup> at a thickness of 550 nm. It is associated with a rise in the rate at which electron-hole pairs are created within the absorber layer and are collected at the output terminals. In Figure 5(c) and 5(d), it is noted that  $V_{oc}$  is recorded as 0.96 V,  $J_{sc}$  is determined to be 32.94 mA/cm<sup>2</sup>, and  $FF$  is found to be 82.03%. Consequently, the device's PCE reaches its peak value of 26.09%, corresponding to an optimized absorber layer thickness of approximately 550 nm. The  $FF$  exhibits a consistent decrease as the thickness of the absorber layer increases, starting at its peak value of 82.03%.  $FF$  is mostly linked to parasitic resistances and the shape of the J–V curve [31]. Because resistance rises as the thickness of the absorber layer increases, as a result,  $FF$  decreases.

As the thickness of the CH<sub>3</sub>NH<sub>3</sub>SnI<sub>3</sub> absorber increases during batch simulation, the  $V_{oc}$  decreases as seen in Figure 5(b). This is because the absorber material undergoes more recombination since charge carriers have a shorter lifetime. Charge carriers generated within the core of the CH<sub>3</sub>NH<sub>3</sub>SnI<sub>3</sub> layer recombine when the thick absorber layer of PSC exceeds the diffusion length. Additionally,

increasing the thickness of the absorber layer reduces the effective bandgap, which sharply reduces the  $V_{oc}$  [32]. Furthermore, according to studies by Pazos-Outón et al. [33] and Slami et al. [34], Equation (4) demonstrates that a change in the short-circuit current ( $J_{sc}$ ) is proportionate to a drop in the open-circuit voltage ( $V_{oc}$ ). This formula is dependent on the absorber layer's thickness and looks like this:

$$V_{oc} = \frac{k_b T}{q} \ln \left[ \frac{J_{sc}}{J_o} + 1 \right] \tag{4}$$

As  $T$  is the operating temperature,  $k_b$  is the Boltzmann constant,  $q$  is the electronic charge,  $J_o$  is the reverse saturation current, and  $J_{sc}$  is the short-circuit current density. The absorber layer is predicted to be 550 nm thick, and this is also the largest PCE value.

### 3.3. Influence of hole transport material and ETM thickness layers

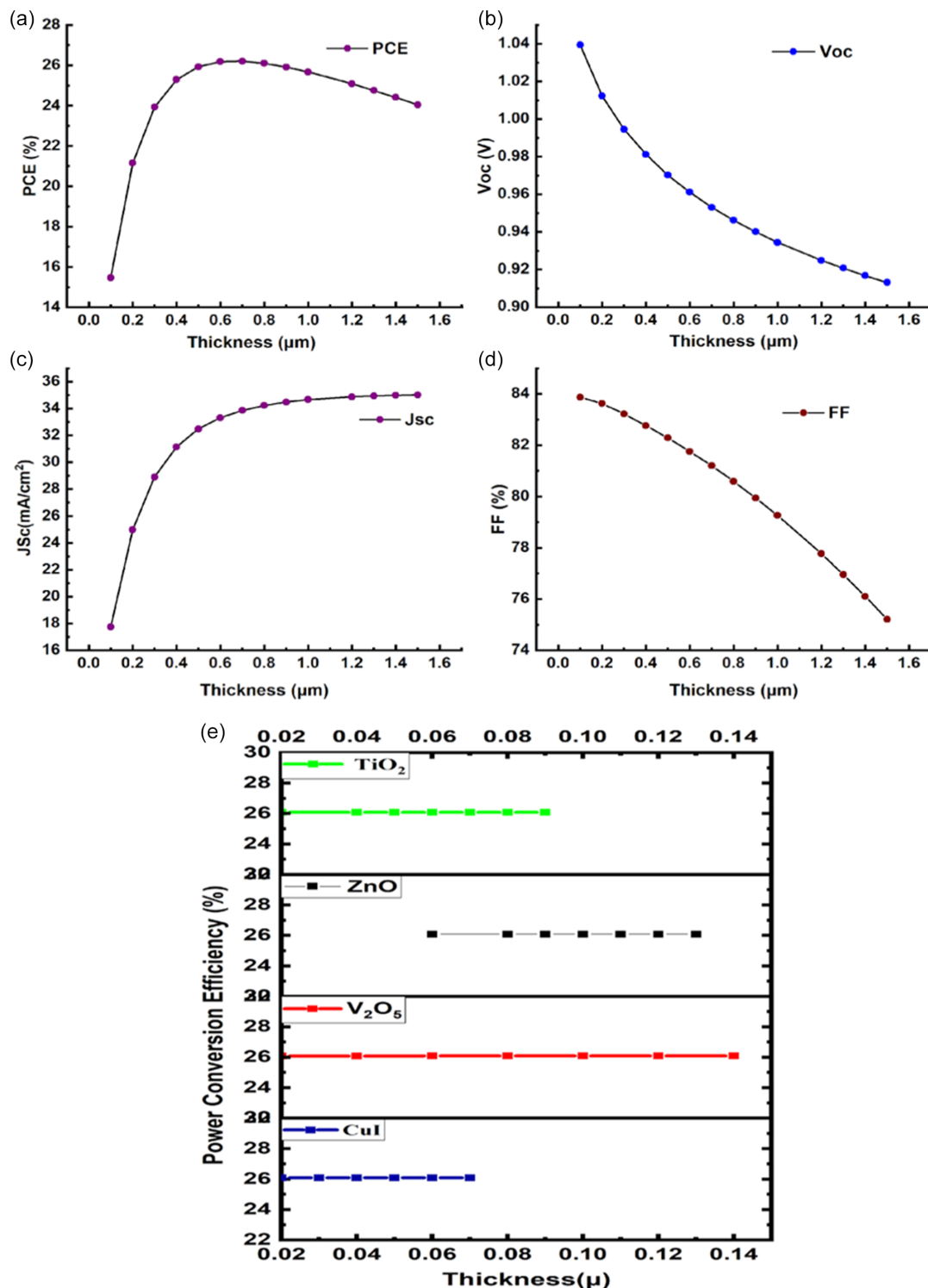
Despite differences in the thickness of ETM and hole transport material ranging from 0.02 μm to 1.4 μm, the absorber layer thickness has stayed constant at 550 nm. The results shown in Figure 5(e) suggest that there does not seem to be any significant influence in this specific range [35]. The further investigation considers this optimization. Since the PCE is maximum at this material thickness, 550 nm is considered the ideal thickness for the absorber layer. The suggested gadget will be further optimized with this optimization in mind.

### 3.4. Temperature's impact on the properties of the device

Understanding solar cell performance at elevated temperatures is crucial for analyzing and ensuring efficiency and stability. At high temperatures, material properties including carrier concentration,

Figure 5

Perovskite layer thickness effect on (a) power conversion efficiency (*PCE*), (b) open circuit voltage ( $V_{oc}$ ), (c) the short circuit current density ( $J_{sc}$ ), and (d) fill factor (*FF*). (e) Effect of ETL and HTL thicknesses on device *PCE*



bandgap, electron and hole mobility, and density of states change. Interlayer deformation results from these changes, which also affect device efficiency and stability. The reduction in efficiency with increasing temperature can be ascribed to a decrease in the diffusion length of charge carriers. Current research indicates that as temperature rises, there is a corresponding increase in force on the layers. This heightened stress results in the formation of

interfacial defects and a decrease in the interconnectivity between the layers [34, 36, 37].

In order to look at how temperature changes affect PSCs' PCE, optimal thicknesses of all layers were employed in this phase of the simulations: ETL (FTO, 400 nm; ZnO, 90 nm;  $\text{TiO}_2$ , 50 nm), perovskite absorber ( $\text{CH}_3\text{NH}_3\text{SnI}_3$ : 550 nm), and HTL ( $\text{V}_2\text{O}_5$ , 100 nm; CuI, 20 nm).

Figure 6 shows how temperature has an impact on PCE,  $FF$ ,  $V_{oc}$ , and  $J_{sc}$ . Since the intensity of incoming light directly affects the current density ( $J_{sc}$ ), an increase in temperature was expected to have a similar effect on  $J_{sc}$ . The link between temperature and  $FF$  is seen in Figure 6(b), where an increase in temperature results in a reduction in  $FF$ . The increase in series resistances and recombination rate that happens at higher temperatures is what causes this drop [38]. There is a direct correlation between the forward voltage drop ( $FF$ ) and the series resistance in an electrical circuit.

$$FF = FF_0 \times \left(1 - \frac{R_s}{R_{CH}}\right) = FF_0 \times \left(1 - \frac{R_s I_{sc}}{V_{oc}}\right) \quad (5)$$

Although thermal generation causes a slight increase in  $J_{sc}$ , as shown in Figure 6(a) and 6(b), the loss in  $V_{oc}$  exceeds the rate of  $J_{sc}$  increase, leading to a decline in efficiency. By raising the temperature to 300 K, the simulation results are improved and the cell's efficiency is increased.

### 3.5. Amphoteric defect density's effect

The absorber layer is a PSC's primary layer. In the bulk of solar processes, the active layer is where recombination, transportation, and generation occur [39, 40]. Different kinds of conductivity are seen in the  $\text{CH}_3\text{NH}_3\text{SnI}_3$  layer, depending on the deposition characteristics of Sn and halide molecules. Furthermore, the  $\text{Sn}^{2+}$  cation is highly susceptible to oxidation during the fabrication process, resulting in defects within the perovskite structure [41, 42]. Thus, imperfections in a solar cell's absorber layer determine electron-hole pair diffusion length and  $V_{oc}$ . The density must be adjusted to maximize perovskite device efficiency. In this work, the amphoteric defect with uniform energy distribution above the absorber layer's  $E_v$  was investigated. The defect states ranged from  $10^{14} \text{ cm}^{-3}$  to  $10^{17} \text{ cm}^{-3}$ . The solar cell performs much better at a low defect density of  $3 \times 10^{14} \text{ cm}^{-3}$ , with PCE of 26.09%,  $V_{oc}$  of 0.96 V,  $J_{sc}$  of  $32.94 \text{ mA/cm}^2$ , and  $FF$  of 82.03% in comparison to early results. The rise in defect density up to  $10^{15} \text{ cm}^{-3}$  barely affects all simulated parameters. Figure 7 shows that all metrics drop drastically as defect density increases beyond  $10^{15} \text{ cm}^{-3}$ . Shown in Figure 8, photovoltaic performance, photo-generated carrier lifetime, and diffusion length depend on absorber defect density.

The influence of the defect density in the perovskite absorber layer on the power conversion is explained by the Shockley-Read-Hall recombination model efficiency (PCE) of solar cells [43, 44].

$$R = \frac{np - n_i^2}{\tau_p \left( n + N_c e^{-\frac{(E_g - E_t)}{k_B T}} \right) + \tau_n \left( p + N_v e^{\frac{E_t}{k_B T}} \right)} \quad (6)$$

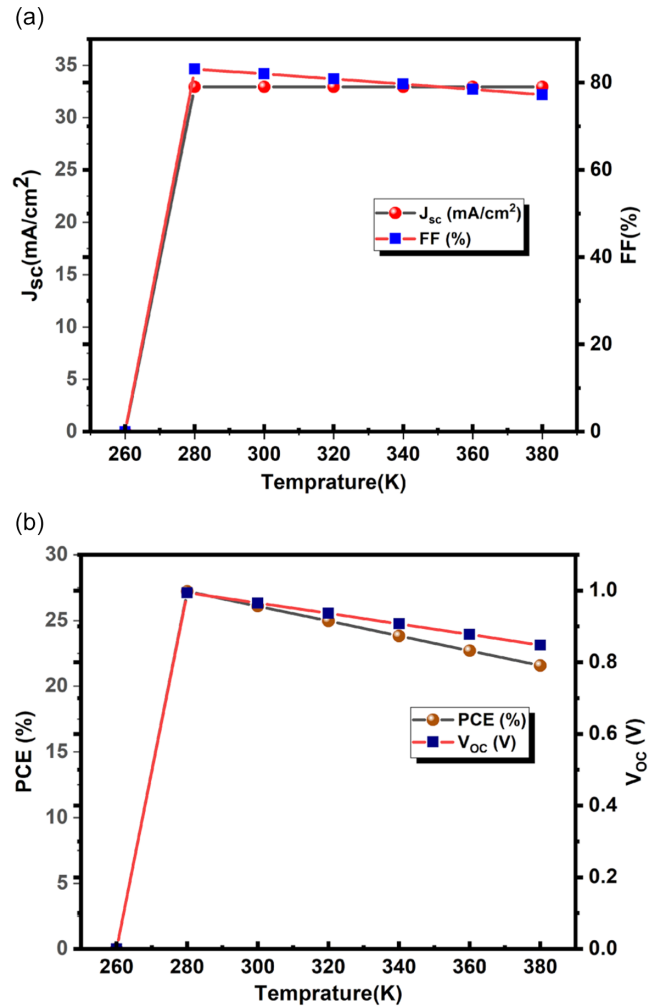
Here, the energy level connected to the trap faults is shown by  $(E_t)$ . The variables  $(p)$  and  $(n)$  represent the densities of mobile holes and electrons, respectively. It is possible to calculate the lifespan of electrons and holes, represented as  $(\tau)$ , as mentioned in Takahashi et al. [45].

$$\tau_{n,p} = \frac{1}{\sigma_{n,p} \cdot v_{th} \cdot N_t} \quad (7)$$

where  $\sigma_{n,p}$  is the capture cross-section area for the electrons and holes,  $N_t$  is the density of the trap defect, and  $v_{th}$  is the thermal velocity.

Figure 6

(a) Effect of temperature on  $J_{sc}$  and  $FF$ . (b) Effect of temperature on  $V_{oc}$  and PCE



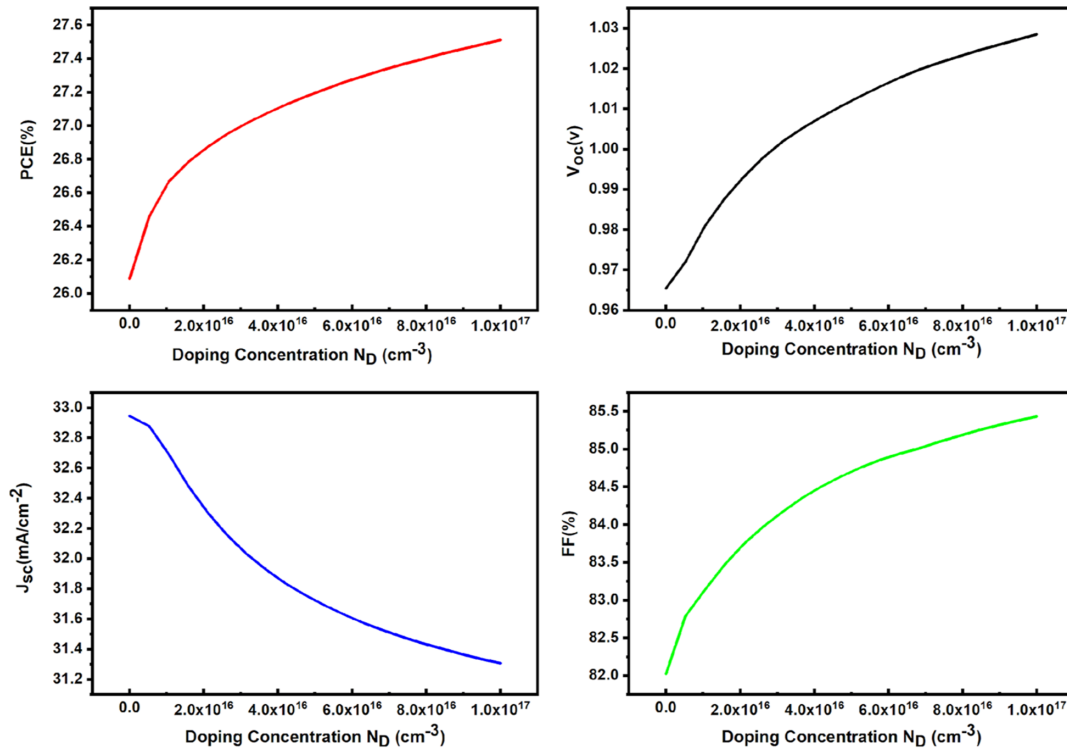
### 3.6. Effect on absorber's layer by doping concentration

Doping is a major factor in improving the efficiency of solar cells. P-type and N-type doping are the two primary categories of doping, which are defined by the particular dopants used [46]. One can self-dope the absorber layer for either n- or p-type doping. Current research indicates that the use of performance-enhancing drugs, often known as doping, has been discovered to aid in the stability of PSCs that can increase their PCE, as several researches have shown [47–49].

In order to investigate the impact of doping concentration on the basics of solar cells, the doping level in the absorber layer was systematically varied within a certain range of  $1 \times 10^{13} \text{ cm}^{-3}$  to  $1 \times 10^{17} \text{ cm}^{-3}$ .

Figure 7 shows how absorber layer doping concentration affects solar cell properties. Doping concentration greatly affects simulated performance measures. The graph illustrates that there is a little impact on parameter variation within the range of  $1 \times 10^{13}$  to  $1 \times 10^{16}$ . This implies that a wide variety of doping optimization possibilities in the absorber layer may be investigated while preserving superior stability. Increased doping density exceeding

**Figure 7**  
Influence of concentration of doping the absorber layer's ND



$1 \times 10^{16} \text{ cm}^{-3}$  leads to higher  $V_{oc}$ . Figure 9 shows that doping density affects solar cell efficiency depending on the level. An increase in charge carrier concentrations is observed in conjunction with the augmentation of doping density at a modest level, which frequently leads to enhancements in cell performance. The phenomenon of exponential decay in  $J_{sc}$  can be observed due to the presence of a tiny depletion region in charge carriers at high doping levels, which hinders efficient carrier collection [50, 51]. The alteration of the

perovskite conductivity behavior resulted in a simultaneous rise in the  $V_{oc}$  and  $J_{sc}$ .

### 3.7. The interface defect layers $\text{CH}_3\text{NH}_3\text{SnI}_3/\text{ZnO}$ and $\text{V}_2\text{O}_5/\text{CH}_3\text{NH}_3\text{SnI}_3$ are in a defect condition

In the suggested non-inverted PSC structure simulations, two defect layers have been taken into account. Using numerical inquiry and batch simulation, defect density at the interface around  $\text{V}_2\text{O}_5/\text{CH}_3\text{NH}_3\text{SnI}_3$  and  $\text{CH}_3\text{NH}_3\text{SnBr}_3/\text{ZnO}$  has been examined. The defect density ranges from  $1 \times 10^{10} \text{ cm}^{-3}$  to  $1 \times 10^{18} \text{ cm}^{-3}$ . Figure 9 and Figure 10 illustrate how interface fault density affects PV characteristic parameters.

As fault density increases, the recombination rate decreases efficiency substantially. The device simulation process is suitable with an interface fault density of  $11 \times 10^{10} \text{ cm}^{-3}$ , as per simulation results.

### 3.8. Effect of different back contact material

Copper (Cu) and others like silver (Ag), gold (Au), tin (Sn), and iron (Fe) have all been used in simulations for non-inverted PSC as back contacts shown in Table 2.

The PCE of several back contact materials is shown in Figure 11. When the selected metal's work function rises, solar cells perform better. Table 2 shows how different metal connections affect the efficiency of the cell. It has been shown that copper (Cu) with a specific work function of five electron volts (eV) exhibits the best properties as a back contact in the context of non-inverted PSCs.

The proposed PSC's J-V characteristic curves are displayed in Figure 12, along with a comparison to other published simulated

**Figure 8**

Impact of absorber layer's overall fault density on PCE (%)

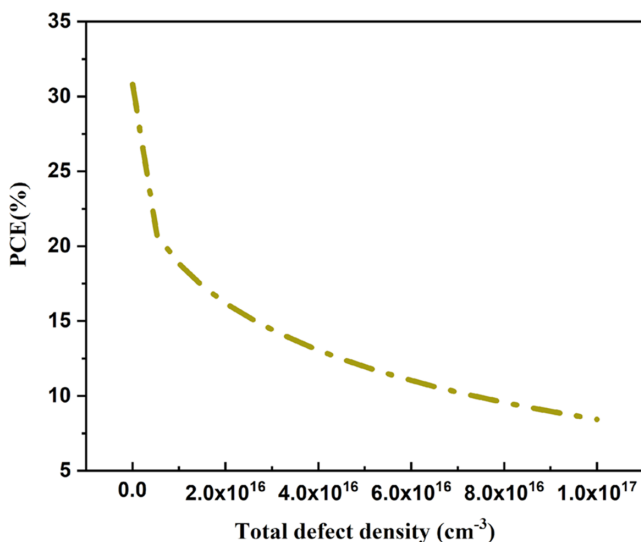


**Figure 9**  
Impact of the condition of the interaction on layer  $\text{CH}_3\text{NH}_3\text{SnI}_3/\text{V}_2\text{O}_5$

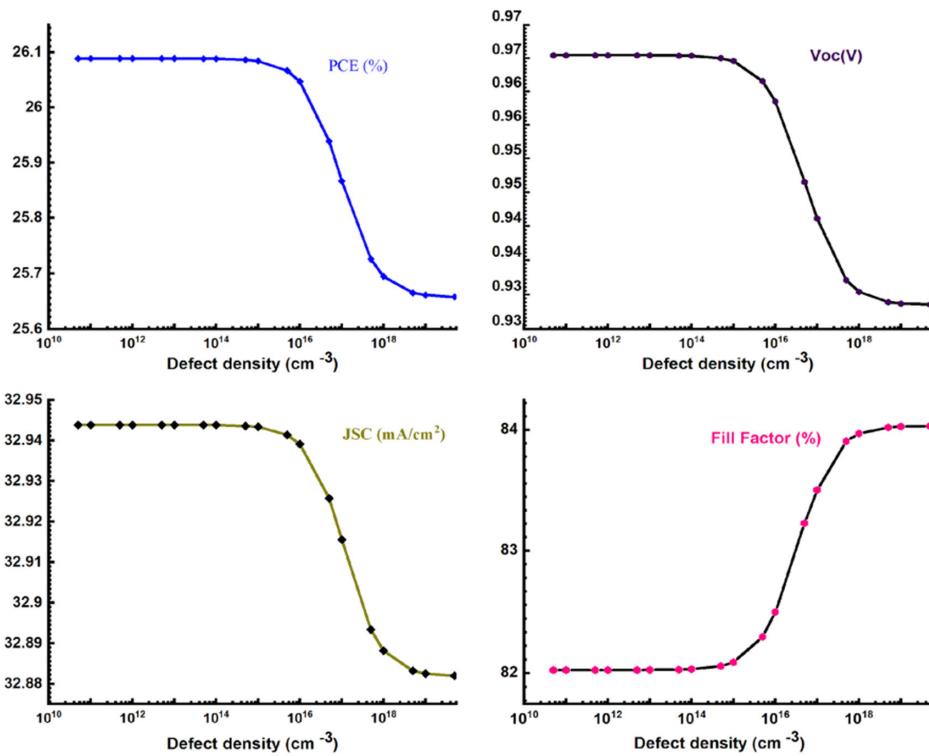


**Figure 10**  
Error's impact interface condition on layer  $\text{CH}_3\text{NH}_3\text{SnI}_3/\text{ZnO}$

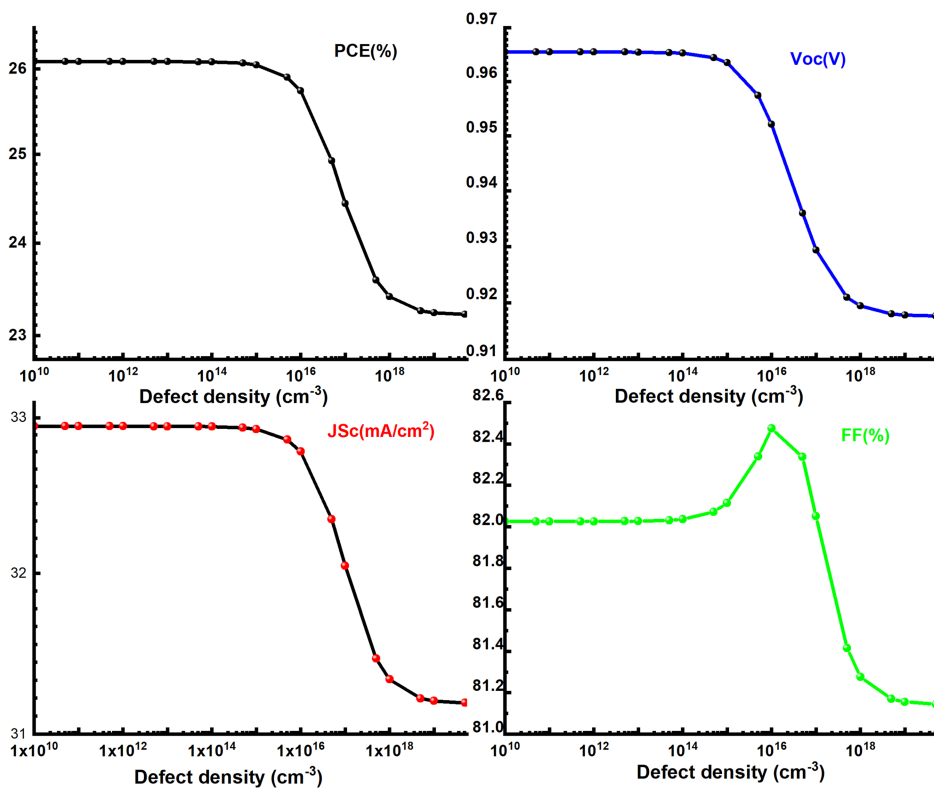


**Figure 11**  
Effects on the efficiency of different back contact metals

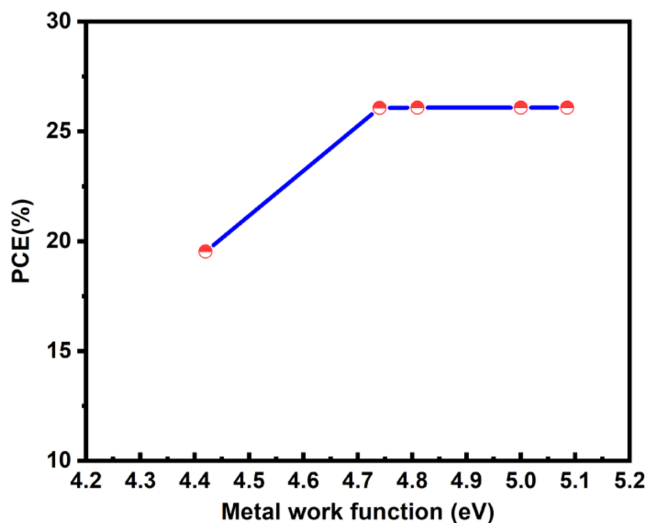


**Figure 12**  
Comparison of current study with reported models

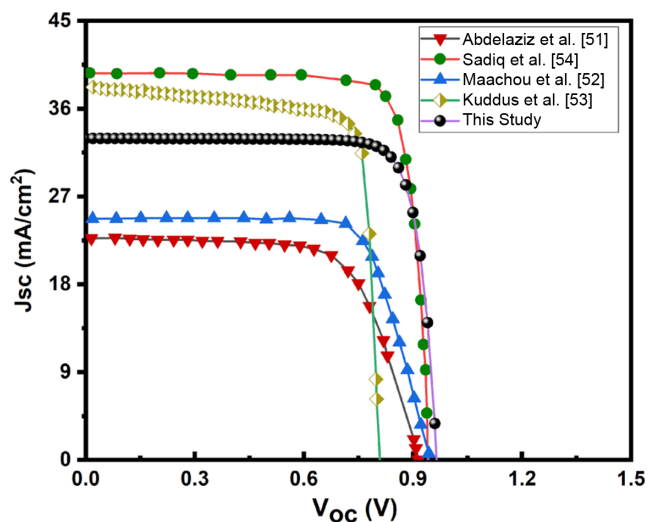


**Figure 13**  
Current study with structure containing double ETLs. (a) PCBM/ZnO, ZnO/SnO<sub>2</sub> and HTLs, and (b) CuI/Spiro-OMeTAD, CuI/PEDOT:PSS

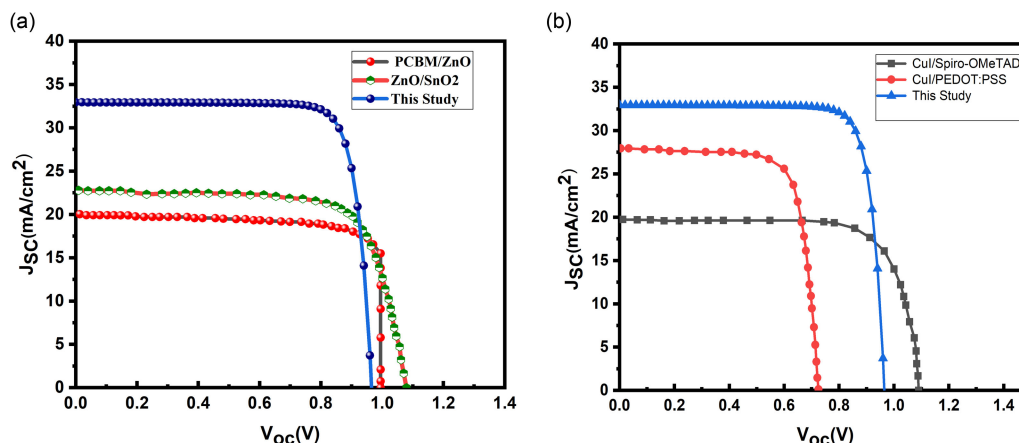


**Table 3**  
Contrast of CH<sub>3</sub>NH<sub>3</sub>SnI<sub>3</sub> model with other study

Model	$V_{oc}$ (V)	$J_{sc}$ (mA/cm <sup>2</sup> )	FF (%)	PCE (%)
Abdelaziz et al. [51]	0.92	22.65	67.74	14.03
Maachou et al. [52]	0.99	25.2	74.1	18.6
Kuddus et al. [53]	0.81	38.51	80.1	24.98
Sadiq et al. [54]	0.95	39.6	83.6	31.4
This study	0.96	32.94	82.03	26.09

models. The explanation for the 31% higher value of  $J_{sc}$  than that reported by Maachou et al. [52] is the 36% thinner absorber layer. Additionally, as indicated by Kuddus et al. [53] and Sadiq et al. [54] for tri-layers, the employment of several layers of ETL and HTL is associated with the increased value of  $J_{sc}$ . The  $V_{oc}$  and literature are similar; additionally, Table 3 compares the electrical parameter values of the suggested model with previous research. Moreover, the comparison of this model's IV characteristic with the double ETLs of PCBM/ZnO and ZnO/SnO<sub>2</sub> and HTLs of CuI/Spiro-OMeTAD is shown in Figure 13.

#### 4. Conclusions

An environmentally friendly lead-free non-inverted PSC device structure was modeled and simulated using SCAPS-1D with CH<sub>3</sub>NH<sub>3</sub>SnI<sub>3</sub> as the absorber layer and two layers of ETL (TiO<sub>2</sub>, ZnO) and HTL (CuI, V<sub>2</sub>O<sub>5</sub>). Each layer's thickness was varied to see how it affected  $J_{sc}$ ,  $V_{oc}$ , PCE, and FF. The proposed model has an open-circuit voltage of 0.96 V, a FF of 82.03%, a PCE of 26.09%, and a  $J_{sc}$  of 32.94 under standard AM 1.5 G circumstances.

The simulation identifies 550 nm as the ideal active layer thickness. The simulation findings showed that temperature, overall defect density, and interface layer defect density (CH<sub>3</sub>NH<sub>3</sub>SnI<sub>3</sub>/ZnO and V<sub>2</sub>O<sub>5</sub>/CH<sub>3</sub>NH<sub>3</sub>SnI<sub>3</sub>) all affected efficiency. Back contact metals were evaluated for PCE (%) with greater variance. The numerical analysis of the suggested structure, as described in this study, produces the following summary: FTO/CuI/V<sub>2</sub>O<sub>5</sub>, CH<sub>3</sub>NH<sub>3</sub>SnI<sub>3</sub>/ZnO/TiO<sub>2</sub>/Cu. The non-inverted structure of polycrystalline PSCs offers a viable lead-free alternative to metal halide perovskites. Additionally, experimentalists benefit from the beneficial support provided by the theoretical insights revealed in this work in several

important areas. By being explicit experimentalists can better understand how these characteristics affect PSC performance with the aid of the theoretical framework. This knowledge makes it a viable option for creating affordable, highly effective PSCs by enabling more informed material selection and appropriate device design.

### Ethical Statement

This study does not contain any studies with human or animal subjects performed by any of the authors.

### Conflicts of Interest

The authors declare that they have no conflicts of interest to this work.

### Data Availability Statement

Upon request, the appropriate author can have access to the data that supported the investigation's findings.

### Author Contribution Statement

**Shahid Farhan:** Conceptualization, Methodology, Software, Validation. **M. Qasim Shah:** Formal analysis, Investigation, Resources. **M. Naeem Khan:** Visualization, Project administration. **M. Arif:** Supervision. **Asim Ghafoor:** Data curation, Writing – original draft, Writing – review & editing.

### References

- [1] Green, M. A., Ho-Baillie, A., & Snaith, H. J. (2014). The emergence of perovskite solar cells. *Nature Photonics*, 8(7), 506–514. <https://doi.org/10.1038/nphoton.2014.134>
- [2] Yoshikawa, K., Kawasaki, H., Yoshida, W., Irie, T., Konishi, K., Nakano, K., . . . , & Yamamoto, K. (2017). Silicon heterojunction solar cell with interdigitated back contacts for a photoconversion efficiency over 26%. *Nature Energy*, 2(5), 17032. <https://doi.org/10.1038/nenergy.2017.32>
- [3] Shi, Z., & Jayatissa, A. H. (2018). Perovskites-based solar cells: A review of recent progress, materials and processing methods. *Materials*, 11(5), 729. <https://doi.org/10.3390/ma11050729>
- [4] Rech, B., Repmann, T., van den Donker, M. N., Berginski, M., Kilper, T., Hüpkes, J., . . . , & Wieder, S. (2006). Challenges in microcrystalline silicon based solar cell technology. *Thin Solid Films*, 511–512, 548–555. <https://doi.org/10.1016/j.tsf.2005.12.161>
- [5] Shah, M. Q., Shafiq, M., Naeem, A., Murtaza, G., Ayyaz, A., Usman, A., . . . , & El-Sheikh, M. A. (2024). Effect of position occupancy of different elements on the structural stability, optoelectronic, thermoelectric and elastic properties of Cs<sub>2</sub>CuAsX<sub>6</sub> (X: Cl, Br, I) halide double perovskite: DFT analysis. *Materials Science in Semiconductor Processing*, 174, 108187. <https://doi.org/10.1016/j.mssp.2024.108187>
- [6] Green, M., Dunlop, E., Hohl-Ebinger, J., Yoshita, M., Kopidakis, N., & Hao, X. (2021). Solar cell efficiency tables (version 57). *Progress in Photovoltaics: Research and Applications*, 29(1), 3–15. <https://doi.org/10.1002/pip.3371>
- [7] Kojima, A., Teshima, K., Shirai, Y., & Miyasaka, T. (2009). Organometal halide perovskites as visible-light sensitizers for photovoltaic cells. *Journal of the American Chemical Society*, 131(17), 6050–6051. <https://doi.org/10.1021/ja809598r>
- [8] Al-Shami, A., Lakhali, M., Hamedoun, M., El Kenz, A., Benyoussef, A., Loulidi, M., . . . , & Mounkachi, O. (2018). Tuning the optical and electrical properties of orthorhombic hybrid perovskite CH<sub>3</sub>NH<sub>3</sub>PbI<sub>3</sub> by first-principles simulations: Strain-engineering. *Solar Energy Materials and Solar Cells*, 180, 266–270. <https://doi.org/10.1016/j.solmat.2017.06.047>
- [9] Alidaei, M., Izadifard, M., Ghazi, M. E., & Ahmadi, V. (2018). Efficiency enhancement of perovskite solar cells using structural and morphological improvement of CH<sub>3</sub>NH<sub>3</sub>PbI<sub>3</sub> absorber layers. *Materials Research Express*, 5(1), 016412. <https://doi.org/10.1088/2053-1591/aaa616>
- [10] Liu, C., Fan, J., Li, H., Zhang, C., & Mai, Y. (2016). Highly efficient perovskite solar cells with substantial reduction of lead content. *Scientific Reports*, 6(1), 35705. <https://doi.org/10.1038/srep35705>
- [11] Iefanova, A., Adhikari, N., Dubey, A., Khatiwada, D., & Qiao, Q. (2016). Lead free CH<sub>3</sub>NH<sub>3</sub>SnI<sub>3</sub> perovskite thin-film with p-type semiconducting nature and metal-like conductivity. *AIP Advances*, 6(8), 085312. <https://doi.org/10.1063/1.4961463>
- [12] Shah, M. Q., Murtaza, G., Shafiq, M., Sharif, S., & Morley, N. A. (2023). Investigation of optoelectronic & thermoelectric features of ZnCrX<sub>2</sub> (X=S Se Te) chalcopyrite semiconductor using mBJ potential. *Chinese Journal of Physics*, 85, 1–14. <https://doi.org/10.1016/j.cjph.2023.05.016>
- [13] Yang, B., Dyck, O., Poplawsky, J., Keum, J., Poretzky, A., Das, S., . . . , & Xiao, K. (2015). Perovskite solar cells with near 100% internal quantum efficiency based on large single crystalline grains and vertical bulk heterojunctions. *Journal of the American Chemical Society*, 137(29), 9210–9213. <https://doi.org/10.1021/jacs.5b03144>
- [14] Fatema, K., & Arefin, M. S. (2022). Enhancing the efficiency of Pb-based and Sn-based perovskite solar cell by applying different ETL and HTL using SCAPS-ID. *Optical Materials*, 125, 112036. <https://doi.org/10.1016/j.optmat.2022.112036>
- [15] Mhamad, S. A., Mohammed, A. M., Aziz, M., & Aziz, F. (2019). Impact of electron transport layers (ETLs) and hole transport layer (HTLs) on perovskite solar cells performance. In T. A. Atesin, S. Bashir & J. L. Liu (Eds.), *Nanostructured materials for next-generation energy storage and conversion: Photovoltaic and solar energy* (pp. 227–246). Springer. [https://doi.org/10.1007/978-3-662-59594-7\\_8](https://doi.org/10.1007/978-3-662-59594-7_8)
- [16] Montoya de los Santos, I., Cortina-Marrero, H. J., Ruiz-Sánchez, M. A., Hechavarría-Difur, L., Sánchez-Rodríguez, F. J., Courel, M., & Hu, H. (2020). Optimization of CH<sub>3</sub>NH<sub>3</sub>PbI<sub>3</sub> perovskite solar cells: A theoretical and experimental study. *Solar Energy*, 199, 198–205. <https://doi.org/10.1016/j.solener.2020.02.026>
- [17] An, Q., Fassel, P., Hofstetter, Y. J., Becker-Koch, D., Bausch, A., Hopkinson, P. E., & Vaynzof, Y. (2017). High performance planar perovskite solar cells by ZnO electron transport layer engineering. *Nano Energy*, 39, 400–408. <https://doi.org/10.1016/j.nanoen.2017.07.013>
- [18] Qiu, W., Buffière, M., Brammertz, G., Paetzold, U. W., Froyen, L., Heremans, P., & Cheyens, D. (2015). High efficiency perovskite solar cells using a PCBM/ZnO double electron transport layer and a short air-aging step. *Organic Electronics*, 26, 30–35. <https://doi.org/10.1016/j.orgel.2015.06.046>
- [19] Bansal, S., & Aryal, P. (2016). Evaluation of new materials for electron and hole transport layers in perovskite-based solar cells through SCAPS-ID simulations. In *IEEE 43rd Photovoltaic*

- Specialists Conference*, 0747–0750. <https://doi.org/10.1109/PVSC.2016.7749702>
- [20] Ashassi-Sorkhabi, H., & Salehi-Abar, P. (2018). Design of two novel hole transport materials via replacing the core of spiro-OMeTAD with tetrathiafulvalene and tetraazafulvalene for application in perovskite solar cells. *Solar Energy*, 173, 132–138. <https://doi.org/10.1016/j.solener.2018.07.047>
- [21] Shafiq, M., Murtaza, G., Shah, M. Q., Raza, H. H., & Ayyaz, A. (2023). Structural, elastic, electronic, optical and thermoelectric properties of metal based ternary chalcopyrite semiconductor for photovoltaic application: First-principles studies. *Optik*, 295, 171502. <https://doi.org/10.1016/j.ijleo.2023.171502>
- [22] Kumar, A., Gupta, U., Tanya, Chaujar, R., Tripathi, M. M., & Gupta, N. (2021). Simulation of perovskite solar cell employing ZnO as electron transport layer (ETL) for improved efficiency. *Materials Today: Proceedings*, 46, 1684–1687. <https://doi.org/10.1016/j.matpr.2020.07.267>
- [23] Zafar, M., Yun, J. Y., & Kim, D. H. (2017). Highly stable inverted organic photovoltaic cells with a V<sub>2</sub>O<sub>5</sub> hole transport layer. *Korean Journal of Chemical Engineering*, 34(5), 1504–1508. <https://doi.org/10.1007/s11814-017-0043-z>
- [24] Lu, C., Zhang, W., Jiang, Z., Zhang, Y., & Ni, C. (2021). CuI/Spiro-OMeTAD double-layer hole transport layer to improve photovoltaic performance of perovskite solar cells. *Coatings*, 11(8), 978. <https://doi.org/10.3390/coatings11080978>
- [25] Di Giacomo, F., Fakharuddin, A., Jose, R., & Brown, T. M. (2016). Progress, challenges and perspectives in flexible perovskite solar cells. *Energy & Environmental Science*, 9(10), 3007–3035. <https://doi.org/10.1039/C6EE01137C>
- [26] Ali, M. A., & Naqib, S. H. (2020). Recently synthesized (Ti<sub>1-x</sub>Mo<sub>x</sub>)<sub>2</sub>AlC (0 ≤ x ≤ 0.20) solid solutions: Deciphering the structural, electronic, mechanical and thermodynamic properties via *ab initio* simulations. *RSC Advances*, 10(52), 31535–31546. <https://doi.org/10.1039/D0RA06435A>
- [27] Zhao, Q., Zhou, B., Hu, Y., Luo, L., Duan, Z., Xie, Z., & Yang, X. (2022). A study on numerical simulation optimization of perovskite solar cell based on CuI and C60. *Materials Research Express*, 9(3), 036401. <https://doi.org/10.1088/2053-1591/ac5a34>
- [28] Shamna, M. S., Nithya, K. S., & Sudheer, K. S. (2020). Simulation and optimization of CH<sub>3</sub>NH<sub>3</sub>SnI<sub>3</sub> based inverted perovskite solar cell with NiO as hole transport material. *Materials Today: Proceedings*, 33, 1246–1251. <https://doi.org/10.1016/j.matpr.2020.03.488>
- [29] Barhoumi, M., Bouzidi, S., Sfina, N., & Bouelnor, G. A. A. (2023). First-principles calculations to investigate electronic and optical properties of Ti<sub>4</sub>GaPbX<sub>2</sub> (X = C or N) two-dimensional materials. *Chemical Physics*, 564, 111728. <https://doi.org/10.1016/j.chemphys.2022.111728>
- [30] Burgelman, M., Decock, K., Niemegeers, A., Verschraegen, J., & Degraeve, S. (2024). *SCAPS manual*. Retrieved from: <https://users.elis.ugent.be/ELISgroups/solar/projects/scaps/SCAPS%20manual%20most%20recent.pdf>
- [31] Liu, D., Wang, Q., Traverse, C. J., Yang, C., Young, M., Kuttipillai, P. S., . . . , & Lunt, R. R. (2018). Impact of ultrathin C<sub>60</sub> on perovskite photovoltaic devices. *ACS Nano*, 12(1), 876–883. <https://doi.org/10.1021/acsnano.7b08561>
- [32] Mandadapu, U., Vedanayakam, S. V., Thyagarajan, K., Reddy, M. R., & Babu, B. J. (2017). Design and simulation of high efficiency tin halide perovskite solar cell. *International Journal of Renewable Energy Research*, 7(4), 1603–1612. <https://doi.org/10.20508/ijrer.v7i4.6182.g7270>
- [33] Pazos-Outón, L. M., Xiao, T. P., & Yablonovitch, E. (2018). Fundamental efficiency limit of lead iodide perovskite solar cells. *The Journal of Physical Chemistry Letters*, 9(7), 1703–1711. <https://doi.org/10.1021/acs.jpcclett.7b03054>
- [34] Slami, A., Bouchaour, M., & Merad, L. (2019). Numerical study of based perovskite solar cells by SCAPS-1D. *International Journal of Energy and Environment*, 13, 17–21.
- [35] Wang, D., Wu, C., Luo, W., Guo, X., Qu, B., Xiao, L., & Chen, Z. (2018). ZnO/SnO<sub>2</sub> double electron transport layer guides open circuit voltage for highly efficient CH<sub>3</sub>NH<sub>3</sub>PbI<sub>3</sub>-based planar perovskite solar cells. *ACS Applied Energy Materials*, 1(5), 2215–2221. <https://doi.org/10.1021/acsaem.8b00293>
- [36] AlZoubi, T., & Moustafa, M. (2019). Numerical optimization of absorber and CdS buffer layers in CIGS solar cells using SCAPS. *International Journal of Smart Grid and Clean Energy*, 8(3), 291–298. <https://doi.org/10.12720/sgce.8.3.291-298>
- [37] Chenene, M. L. (1999). *Fabrication and characterization of CuInSe<sub>2</sub>/CdS/ZnO thin film solar cells*. Master's Thesis, University of Johannesburg.
- [38] Kim, H., Lim, K. G., & Lee, T. W. (2016). Planar heterojunction organometal halide perovskite solar cells: Roles of interfacial layers. *Energy & Environmental Science*, 9(1), 12–30. <https://doi.org/10.1039/C5EE02194D>
- [39] Barbé, J., Tietze, M. L., Neophytou, M., Murali, B., Alarousu, E., Labban, A. E., . . . , & Del Gobbo, S. (2017). Amorphous tin oxide as a low-temperature-processed electron-transport layer for organic and hybrid perovskite solar cells. *ACS Applied Materials & Interfaces*, 9(13), 11828–11836. <https://doi.org/10.1021/acsaami.6b13675>
- [40] Leijtens, T., Prasanna, R., Gold-Parker, A., Toney, M. F., & McGehee, M. D. (2017). Mechanism of tin oxidation and stabilization by lead substitution in tin halide perovskites. *ACS Energy Letters*, 2(9), 2159–2165. <https://doi.org/10.1021/acscenergylett.7b00636>
- [41] Kagan, C. R., Mitzi, D. B., & Dimitrakopoulos, C. D. (1999). Organic-inorganic hybrid materials as semiconducting channels in thin-film field-effect transistors. *Science*, 286(5441), 945–947. <https://doi.org/10.1126/science.286.5441.945>
- [42] Song, J., Hu, W., Li, Z., Wang, X. F., & Tian, W. (2020). A double hole-transport layer strategy toward efficient mixed tin-lead iodide perovskite solar cell. *Solar Energy Materials and Solar Cells*, 207, 110351. <https://doi.org/10.1016/j.solmat.2019.110351>
- [43] Shockley, W., & Read Jr, W. T. (1952). Statistics of the recombinations of holes and electrons. *Physical Review*, 87(5), 835–842. <https://doi.org/10.1103/PhysRev.87.835>
- [44] Baig, F., Khattak, Y. H., Mari, B., Beg, S., Ahmed, A., & Khan, K. (2018). Efficiency enhancement of CH<sub>3</sub>NH<sub>3</sub>SnI<sub>3</sub> solar cells by device modeling. *Journal of Electronic Materials*, 47(9), 5275–5282. <https://doi.org/10.1007/s11664-018-6406-3>
- [45] Takahashi, Y., Hasegawa, H., Takahashi, Y., & Inabe, T. (2013). Hall mobility in tin iodide perovskite CH<sub>3</sub>NH<sub>3</sub>SnI<sub>3</sub>: Evidence for a doped semiconductor. *Journal of Solid State Chemistry*, 205, 39–43. <https://doi.org/10.1016/j.jssc.2013.07.008>
- [46] Bai, Y., Dong, Q., Shao, Y., Deng, Y., Wang, Q., Shen, L., . . . , & Huang, J. (2016). Enhancing stability and efficiency of

- perovskite solar cells with crosslinkable silane-functionalized and doped fullerene. *Nature Communications*, 7(1), 12806. <https://doi.org/10.1038/ncomms12806>
- [47] Xiao, J., Shi, J., Li, D., & Meng, Q. (2015). Perovskite thin-film solar cell: Excitation in photovoltaic science. *Science China Chemistry*, 58(2), 221–238. <https://doi.org/10.1007/s11426-014-5289-2>
- [48] Chowdhury, M. S., Shahahmadi, S. A., Chelvanathan, P., Tiong, S. K., Amin, N., Techato, K. A., . . . , & Suklueng, M. (2020). Effect of deep-level defect density of the absorber layer and n/i interface in perovskite solar cells by SCAPS-1D. *Results in Physics*, 16, 102839. <https://doi.org/10.1016/j.rinp.2019.102839>
- [49] Peter Amalathas, A., Landová, L., Conrad, B., & Holovský, J. (2019). Concentration-dependent impact of alkali Li metal doped mesoporous TiO<sub>2</sub> electron transport layer on the performance of CH<sub>3</sub>NH<sub>3</sub>PbI<sub>3</sub> perovskite solar cells. *The Journal of Physical Chemistry C*, 123(32), 19376–19384. <https://doi.org/10.1021/acs.jpcc.9b05355>
- [50] Zhao, Y., Liang, C., Sun, M., Liu, Q., Zhang, F., Li, D., & He, Z. (2014). Effect of doping on the short-circuit current and open-circuit voltage of polymer solar cells. *Journal of Applied Physics*, 116(15), 154506. <https://doi.org/10.1063/1.4898692>
- [51] Abdelaziz, S., Zekry, A., Shaker, A., & Abouelatta, M. (2020). Investigating the performance of formamidinium tin-based perovskite solar cell by SCAPS device simulation. *Optical Materials*, 101, 109738. <https://doi.org/10.1016/j.optmat.2020.109738>
- [52] Maachou, A., Aboura, H., Amrani, B., Khenata, R., Omran, S. B., & Varshney, D. (2011). Structural stabilities, elastic and thermodynamic properties of Scandium Chalcogenides via first-principles calculations. *Computational Materials Science*, 50(11), 3123–3130. <https://doi.org/10.1016/j.commat.2011.05.038>
- [53] Kuddus, A., Rahman, M. F., Hossain, J., & Ismail, A. B. M. (2020). Enhancement of the performance of CdS/CdTe heterojunction solar cell using TiO<sub>2</sub>/ZnO bi-layer ARC and V<sub>2</sub>O<sub>5</sub> BSF layers: A simulation approach. *The European Physical Journal Applied Physics*, 92(2), 20901. <https://doi.org/10.1051/epjap/2020200213>
- [54] Sadiq, M., Khan, M. N., Arif, M., Naveed, A., Ullah, K., & Afridi, S. (2021). Numerical investigation of a new approach based on perovskite CH<sub>3</sub>NH<sub>3</sub>PbI<sub>3</sub> absorber layer for high-efficiency solar cells. *Materials Research Express*, 8(9), 095507. <https://doi.org/10.1088/2053-1591/ac2377>

**How to Cite:** Farhan, S., Shah, M. Q., Khan, M. N., Arif, M., & Ghafoor, A. (2024). Exploring the Bilayer Approach to Analyzing Lead-Free Perovskite Solar Cells' Numerical Aspects for High Efficiency. *Journal of Optics and Photonics Research*, 1(4), 190–201. <https://doi.org/10.47852/bonviewJOPR42022149>